Nanoscale

Green chemistry and first-principles theory enhance catalysis: Synthesis and 6-fold catalytic activity increase of sub-5 nm Pd and Pt@Pd nanocubes

Journal:	*Nanoscale*
Manuscript ID	NR-ART-04-2022-002278.R1
Article Type:	Paper
Date Submitted by the Author:	14-Jun-2022

Complete List of Authors:	Mastronardi, Valentina; Italian Institute of Technology Kim, Junseok; Pennsylvania State University, Chemical Engineering Veronesi, Marina; Istituto Italiano di Tecnologia, Pharmachemistry Pomili, Tania; Istituto Italiano di Tecnologia Udayan, Gayatri; Istituto Italiano di Tecnologia Center for Biomolecular Nanotechnologies; University of Salento Department of Engineering Innovation Bandiera, Tiziano; Istituto Italiano di Tecnologia, Dept. of Drug Discovery and Development Berti, Francesco; Italian Institute of Technology Diercks, Justus; Paul Scherrer Institut, Electrochemistry Laboratory Herranz, Juan; Paul Scherrer Institut, Electrochemistry Laboratory Brescia, Rosaria; Istituto Italiano di Tecnologia, Electron Microscopy Facility Fichthorn, Kristen; Pennsylvania State University, Chemical Engineering Pompa, Pier; Italian Institute of Technology (IIT), Center for Bio-Molecular Nanotechnology Moglianetti, Mauro ; Italian Institute of Technology, ; HiQ-Nano,

Green chemistry and first-principles theory enhance catalysis: Synthesis and 6-fold catalytic activity increase of sub-5 nm Pd and Pt@Pd nanocubes

Valentina Mastronardi[1,2,⊥], Junseok Kim[3,⊥], Marina Veronesi[4.5], Tania Pomili[1,2], Francesco Berti[4], Gayatri Udayan[6,7], Rosaria Brescia[8], Justus S. Diercks[9], Juan Herranz[9], Tiziano Bandiera[4], Kristen A. Fichthorn[3,*], Pier Paolo Pompa[1], Mauro Moglianetti[1,7,•,*]

1. Nanobiointeractions&Nanodiagnostics, Istituto Italiano di Tecnologia, Via Morego 30 – 16163 Genova, Italy

2. Department of Chemistry and Industrial Chemistry, University of Genova, Via Dodecaneso 31, 16146 Genova, Italy

3. Department of Chemical Engineering, The Pennsylvania State University, University Park, Pennsylvania 16802, United States

4. D3-PharmaChemistry, Istituto Italiano di Tecnologia, 16163 Genoa, Italy

5. Structural Biophysics and Translational Pharmacology Facility, Istituto Italiano di Tecnologia, 16163 Genoa, Italy

6. Department of Engineering for Innovation, University of Salento, Via per Monteroni, 73100 Lecce, Italy

7. Center for Bio-Molecular Nanotechnologies, Istituto Italiano di Tecnologia, Via Barsanti 14 – 73010 Arnesano (Lecce), Italy

8. Electron Microscopy Facility, Istituto Italiano di Tecnologia, Via Morego 30, 16163 Genova, Italy

9. Electrochemistry Laboratory, Paul Scherrer Institut, Forschungsstrasse 111, 5232 Villigen,PSI Switzerland

⊥ Equally Contributing Authors

• Current address: *Institute for the Study on Nanostructured Materials (ISMN), National Research Council (CNR), Via Gobetti 101, 40129 Bologna, Italy*

* mauro.moglianetti@ismn.cnr.it, fichthorn@psu.edu

ABSTRACT

Synthesizing metal nanoparticles with fine control of size, shape and surface properties is of high interest for applications such as catalysis, nanoplasmonics, and fuel cells. In this contribution, we demonstrate that the citrate-coated surfaces of palladium (Pd) and platinum (Pt) @Pd nanocubes with a lateral length <5 nm and low polydispersity in shape achieve superior catalytic properties. The synthesis achieves great control of the nanoparticle's physico-chemical properties by using only biogenic reagents and bromide ions in water while being fast, easy to perform and scalable. The role of the seed morphology is pivotal as Pt single crystal seeds are necessary to achieve low polydispersity in shape and prevent nanorods formation. In addition, electrochemical measurements demonstrate the abundancy of Pd {100} surface facets at a macroscopic level, in line with data inferred from TEM analysis. Quantum density functional theory calculations indicate that the kinetic origin of cubic Pd nanoshapes is facet-selective Pd reduction/deposition on Pd(111). Moreover, we underline both from an experimental and theoretical point of view that bromide alone does not induce nanocube formation without the synergy with formic acid. The superior performance of these highly controlled nanoparticles to perform the catalytic reduction of 4-nitrophenol was proved: polymer-free and surfactant-free Pd nanocubes outperform state-of-the-art materials by a factor > 6 and a commercial Pd/C catalyst by more than one order of magnitude.

INTRODUCTION

The precise control of the size and shape of nanoparticles is a powerful way to govern the properties of nanomaterials and, hence, their performance in a broad range of applications like catalysis, electrocatalysis, and nanomedicine.[1–10] Indeed, for catalytic nanomaterials such as palladium (Pd) and platinum (Pt), the shape, size and presence and nature of surface coatings regulate the catalytic activity and selectivity.[11–15] For example, it has been demonstrated that the size and shape of Pd nanomaterials have a profound effect on several reactions, such as carbon–carbon cross coupling, reduction of nitroarenes, CO oxidation and CO_2 hydrogenation[16–18]. These recent data show that the performance of a nanocatalyst can be substantially enhanced by rational design and achieving strict control of both dimension and shape.[11,19] Moreover, a few recent reports have started to elucidate the role of the surface structure achieved by shape-controlled syntheses on the catalytic performance. Pd nanocubes with dimension above 100 nm proved as an efficient catalyst for cross-coupling reactions and for nitrophenol reduction whilst providing greater stability and higher selectivity with enhanced recyclability.[20] Also in the attempt to find alternatives to fossil fuels by developing viable fuel cells, the surface structure of Pd catalysts is a critical point to achieve highly improved efficiency and market performance requirements for direct formic acid fuel cells.[21,22] Indeed, from the studies on single-crystal Pd electrodes, the effect of surface structure has been elucidated, showing that the current density reaches a maximum value for Pd(100).[23]

Major challenges need to be overcome to develop Pd nanomaterials in a sustainable manner without the use of high temperatures, organic solvents, dry argon, and/or expensive metal derivatives. Indeed, the development of a direct synthesis of well-controlled Pd NPs stabilized in water will open the way to the direct use of the catalyst at extremely low loading.[24] Furthermore, the use of easy-to-remove coating enables the surface functionalization with amphiphilic compounds for an efficient phase exchange during catalysis. Alternatively, the use of green bio-reductants, which also act as stabilizers, has been proposed as an economical and environmental solution but reproducibility issues and a high variability in the bio-extract composition and consequent low catalytic activity hampered their use.[20,24]

In this framework, solution-phase syntheses for the formation of metal particles with sizes below 7 nm with narrow size and shape distributions and a high yield of usable material are challenging. A limiting factor of many synthetic protocols is the use of various surfactants, polymers, and hard templates,[25–28] which can significantly alter the properties of the material[21,24,29–31] and are difficult to remove after synthesis.[32] Here, we present an eco-friendly hydrothermal synthetic method without the use of polymers and surfactants to obtain size-tuneable Pd nanocubes with ultra-small sizes using sodium citrate, formic acid, and potassium bromide.

A key aspect of our synthesis protocol is the use of a weak reducing agent (formic acid) which, in the presence of adsorbed bromide, performs {111} facet-selective, on-surface reduction of Pd metal ions to produce sub-five-nanometer cube-shaped Pd nanocrystals enclosed by {100} facets. Prior experimental studies seemed to indicate that halides[33–35] can function as capping agents for promoting {100}-faceted Pd nanocrystals[36–38] and that halides can affect Pd metal-salt reduction and, hence, influence the nanocrystal growth and shape.[12,34,39–

[42] However, the capping effect of halides has not been fully demonstrated for Pd nanocrystals and the mechanism governing the synergy between halides and Pd salt reduction remains elusive. In this paper, we use first-principles density-functional theory (DFT) to show how synergistic interactions between adsorbed bromide and formic acid reductant can affect the shapes of Pd nanocrystals. Based on these synergistic interactions, we synthesized ultra-small Pd nanocubes using both Pd and Pt seeds. We confirmed by electrochemical measurements the abundancy of Pd {100} surface facets. Moreover, the use of microwave reactor (with a multiple reaction vessels setup) allowed synthesizing more than 100 mg of nanocubes simultaneously in less than an hour. The detailed understanding of the key synthetic parameters together with the easy procedure to control the growth and achieve the desired properties, opens the way to a wide application of these nanomaterials in high-demand catalytic and electrocatalytic processes.

We indeed proved the superior capability of these highly-controlled and high-quality nanoparticles by performing the catalytic reduction of 4-nitrophenol, a reaction extensively used in organic chemistry and industry. We evaluated the performance with nuclear magnetic resonance (NMR) and compared it with a commercial catalyst and the data in the literature, finding that the catalytic activity of Pt@Pd nanocubes is superior by at least a factor of 6 with respect to the best reported[24] results and by more than one order of magnitude compared to the commercial Pd/C catalyst.

EXPERIMENTAL DETAILS

Materials.

Chloroplatinic acid hexahydrate BioXtra, formic acid puriss. p.a., ACS reagent, reag. Ph. Eur., ≥98%**,** Palladium(II) chloride 99.999%, sodium citrate tribasic dihydrate BioUltra, acetic acid puriss. p.a., ACS reagent, reag. ISO, reag. Ph. Eur., ≥99.8%, nitric acid puriss. p.a., ACS reagent, reag. ISO, reag. Ph. Eur., ≥99.8%, L-ascorbic acid BioXtra, potassium bromide BioXtra, ≥99.0%, sodium borohydride, and citric acid anhydrous were bought from Merck/Sigma-Aldrich. Ultrapure water with a resistivity of 18.2 MΩ·cm was used throughout the experiment.

Pd Seed Synthetic Procedure.

Pd seeds were synthesized in aqueous solution (130 mL ultrapure water) with the addition of 85 μL of $PdCl_2$ at 55 mM (previously dissolved in 1.1 M nitric acid solution), followed by 9.5 mL of a solution containing 33 mM sodium citrate and 2.5 mM citric acid. Then, 550 μL of freshly prepared $NaBH_4$ (at a concentration of 25 mM) were added to start the seeds formation. To achieve a fast reduction of the Pd ions and, consequently, a small seed size, the vessel was placed into a glycerol bath already warmed-up at 107 °C. The reaction was kept at these conditions for 12 minutes under magnetic stirring at moderate rate. At the end the vessel was removed from the glycerol bath and left to cool under stirring for an hour.

Pt Seed Synthetic Procedure.

50 μL hexachloroplatinic acid aqueous solution at a concentration of 0.55 M (previously prepared and stored in the fridge) was added to 95 mL ultrapure water, already warmed-up at 90°C into a glycerol bath. After 2 min, 0.5 mL of solution containing sodium citrate at 35 mM and citric acid at 3 mM was added, immediately followed by the addition of 2 mL of freshly prepared $NaBH_4$ (at a concentration of 11mM). After 12 minutes, the solution was cooled to room temperature by removing it from the glycerol bath.

Pd and Pt*@Pd Nanocube Synthetic Procedure.*

$PdCl_2$ was previously dissolved in 1M of CH_3COOH aqueous solution to reach a final concentration of 56.4 mM. 4.5 mL of Pt or Pd seeds were added in a sealed glass container (ACE glass pressure reactor with Teflon cap) followed by 60 mL Ultrapure water with 159 μL of Pd (II) acetate (0.05M) and 1 mL of a solution containing 0.2M formic acid, 0.34M sodium citrate, and 0.5mM L-ascorbic acid. After waiting 1 minute, 1.6 mL of 0.5 M KBr was added in the solution. The vessel was then sealed, placed in a glycerol bath already at 105°C for 3 minutes. The reaction was kept for 12 minutes under stirring at moderate rate. The solution was then cooled to room temperature.

Transmission electron microscopy analyses.

Bright-field transmission electron microscopy (BF-TEM) imaging was carried out in a JEM-1011 microscope (W filament) operated at 100 kV. High-resolution TEM (HR-TEM) and high-angle annular dark-field-scanning TEM (HAADF-STEM) analyses were carried out in an image-Cs-corrected JEM-2200FS instrument, operated at 200 kV. Due to the small size of the nanocrystals and to the fast carbon contamination build-up upon electron-beam irradiation, regions of interest were exposed to a relatively low dose rate (≈70 electrons/(Å2 s)) and HRTEM images were acquired using a direct electron detection camera (K2 Summit, Gatan), in super-resolution mode. Each HRTEM image shown here is extracted from a (140 nm)2 frame. Each of these frames is obtained by summing a stack of aligned frames, each corresponding to a short exposure (0.2 s), with a total acquisition time of 10 s. Compositional mapping was carried out by energy-dispersive X-ray spectroscopy (EDS) coupled with HAADF-STEM imaging, using a Bruker X-Flash 5060 silicon-drift detector (SDD). The compositional maps reported here were obtained by integration of the Lα peaks of Pt and Pd.

Computational Methods

DFT total energy calculations were performed using the Vienna *Ab initio* Simulation Package (VASP) with projector-augmented waves[43–47] and the generalized gradient approximation (GGA) by Perdew, Burke, and Ernzerhof (PBE).[48] The plane-wave basis set energy cut-off was 450 eV and Monkhorst-Pack grids were used for Brillouin zone sampling.[49] To account for long-range van der Waals (vdW) interactions, the DFT-D2 method of Grimme[50] was used. In this method, the cut-off radius was taken to be 40.0 Å, while the dispersion coefficient and the vdW radius from Ruiz et al. were used to account for bulk screening effects.[51] A (15 x 15

x 15) ***k***-point mesh was used to calculate the energy of bulk Pd. The calculated lattice constant was 3.95 Å, in good agreement with other theoretical calculations and slightly higher than the experimental value (3.89 Å).[52–55] To calculate the total energy of an isolated Pd atom, a Br atom, and COOH in the gas phase, we used a cubic unit cell with a side length of 20 Å and a single ***k*** point.

Pd surfaces were represented as periodic slabs with six layers of Pd and adsorbed Br and/or COOH on one side of the slab. The bottom three layers of Pd were fixed to the bulk configuration. Regarding Br adsorption, we found that Br prefers to bind to the fcc hollow sites of Pd(111) and to the four-fold hollow sites of Pd(100). COOH binds to the Pd surface atoms via the C atom. To identify the predominant surface structures for various chemical potentials of Br and COOH on Pd(100) and Pd(111), the surface energy was calculated using

$$\gamma_{\mathrm{Pd-Br-COOH}} = \frac{E_{\mathrm{Pd-Br-COOH}} - N_{\mathrm{Pd}}E_{\mathrm{Pd}}^{\mathrm{Bulk}} - N_{\mathrm{Br}}\mu_{\mathrm{Br^-}} - N_{\mathrm{COOH}}\mu_{\mathrm{COOH}}}{A_{\mathrm{surf}}} - \gamma_{\mathrm{Pd}}^{\mathrm{fixed}} \qquad (1)$$

where $E_{\mathrm{Pd-Br-COOH}}$ is the energy of a Pd slab with absorbed Br and COOH, N_{Pd} and $E_{\mathrm{Pd}}^{\mathrm{Bulk}}$ represent the number of Pd atoms in the Pd slab and the DFT bulk energy per Pd atom, N_{Br} is the number of absorbed Br atoms, $\mu_{\mathrm{Br^-}}$ is the chemical potential of solution phase Br^-, N_{COOH} is the number of absorbed COOH atoms, μ_{COOH} is the chemical potential of COOH, and A_{surf} is the surface area of a Pd slab. Since absorbed species are adsorbed on only one side of the Pd slab, we subtracted $\gamma_{\mathrm{Pd}}^{\mathrm{fixed}}$ – the surface energy of a bare Pd surface slab with atoms fixed at the bulk coordinates.

We carried out convergence tests for the surface energy of 1/4 monolayer (ML) Br on Pd(100). Here, one ML occurs when the ratio of adsorbed species to Pd surface atoms is unity. Convergence tests were performed to test the vacuum spacing, cut-off energy, and ***k***-point mesh using a (2x2) unit cell. The results of these calculations are shown in Table S2. To find an optimal ***k***-point mesh for other unit cells, we performed convergence tests using the same the cut-off energy and vacuum spacing as the optimal values in Table S2. The corresponding optimal ***k***-point meshes used for other unit cell sizes are listed in Table S2. All structures were relaxed until the force acting on all atoms was smaller than 0.01 eV/Å with an energy convergence criterion of 10^{-6} eV.

Deposition of Pd nanocubes on carbon

10 mg of Vulcan XC72R carbon black (Carbon Corp) were added to 20 mL of ultrapure water under moderate stirring condition. Magnetic stirring and ultrasonic bath immersion were alternated for 2.5 h in order to achieve a dispersion of the material in water. After having achieved a black homogenous suspension, Pd NPs solution (at 0.2mg/ml) was added with a loading of 20% w/w and the solution was sonicated for another 20 minutes. After achieving a well-dispersed Pd NPs and Vulcan carbon black solution, NaOH in pellets (around 0.4 g) were added to favor the detachment of citrate from the nanoparticles surface and, hence, the destabilization and consequent precipitation of the composite material overnight. Then, the material was washed at least 5 times with ultrapure water.

Electrochemical characterization

The electrochemical characterization of the Pd-nanocubes and the 10 % Pd/C commercial catalyst used as a benchmark was carried out using thin-film rotating disk electrode (RDE) voltammetry.[56] Inks of the carbon-supported catalysts were prepared by mixing a weighed amount of the powders in a 70:30 volume mixture of ultrapure water (18.2 MΩ·cm, ELGA Purelab Ultra) and isopropanol (Sigma-Aldrich, HPLC grade, 99.9 %), as well as the amount of Nafion perfluorinated resin solution (Sigma-Aldrich, 5 %) necessary to yield a Nafion-to-carbon mass ratio of 0.3. To prepare electrodes with Pd loadings of 10 $\mu g_{Pd} \cdot cm^{-2}$, the catalyst/solvent mixture was carefully sonicated for one minute, and a drop of 8 µL was cast onto a mirror-polished 5 mm diameter glassy carbon disk (HTW Hochtemperatur-Werkstoffe) inserted in a PTFE RDE tip (E5TQ, Pine Research) and dried under a N_2-flow. Electrodes of the unsupported Pd nanocubes were prepared by diluting the aqueous solution in which the nanocubes were dispersed with ultrapure water to yield a Pd-loading of $25 \mu g_{Pd} \cdot cm^{-2}$ upon drop-casting 30µL of solution on the glassy carbon disk and drying under N_2-flow.

The RDE tip was thereafter connected to a shaft (AFE6M, Pine Research) and a rotation controller (Pine Research) and inserted into a custom glass cell (Schmizo AG). The counter and reference electrodes used were a gold mesh (Advent Research Materials) and an Ag/AgCl electrode (Harvard Apparatus, LF-1) pre-calibrated vs. the reversible hydrogen electrode (RHE), respectively. All electrodes were inserted into the potassium phosphate electrolyte and separated using glass compartments with an integrated glass frit (Ametek G0300, 4 mm diameter).

All glassware had been previously cleaned overnight by immersion in a piranha solution consisting of one part of H_2O_2 (30 %, Merck EMSURE) and three parts of H_2SO_4 (96 %, Merck Suprapure), and was thereafter washed with and boiled in ultrapure water multiple times.

The cleaned cell was filled with a total of 50 mL of 0.5 M potassium phosphate buffer (K_2HPO_4/KH_2PO_4) or 0.1 M H_2SO_4 (96 %, VWR, trace analysis) electrolyte saturated with nitrogen (N_2, Carbagas AG, 6.0 quality) constantly supplied through a glass bubbler. The phosphate buffer electrolyte was freshly prepared by mixing 17.146 g of di-potassium hydrogen phosphate (K_2HPO_4, Merck LiChropur, anhydrous, 99.999 %) and 3.615 g potassium dihydrogen phosphate (KH_2PO_4, Merck, LiChropur, anhydrous, 99.999 %) in 250 mL of ultrapure water (18.2 MΩ·cm, ELGA Purelab Ultra). The pH of the electrolyte was repeatedly measured as 7.3 (Metrohm 913 pH meter with Metrohm Unitrode 6.0258.010) when saturated with N_2.

Following the connection of all electrodes to the potentiostat (BioLogic, VSP-300) and the immersion of the RDE, the commercial 10 % Pd/C catalyst was conditioned by recording ten cyclic voltammograms (CVs) at 100 $mV \cdot s^{-1}$, followed by five CVs at 50 $mV \cdot s^{-1}$ and several CVs at 20 and 10 $mV \cdot s^{-1}$ between 0.05 and 1.25 V_{RHE}. In contrast, for the 20 % Pd nanocubes on carbon, the CVs at 100 and 50 $mV \cdot s^{-1}$ were omitted, and the CVs at 20 and 10 $mV \cdot s^{-1}$ were carried out directly in a narrower potential window of 0.05 to 0.7 V_{RHE}, as to prevent the loss of the nanoparticles' shape due to facet recontruction[57]. For the same reason, the unsupported Pd nanocubes were measured in the same potential window at 50 $mV \cdot s^{-1}$, with no previous conditioning cycles

being run. CO-stripping measurements on the carbon-supported materials were started after conditioning was completed by holding the potential for 30 minutes at 0.4 V_{RHE} with a rotation rate of 1600 rpm being applied. During the potential hold, the previously N_2-saturated solution was purged with CO for the first five minutes and the CO was subsequently replaced with N_2 for 25 minutes. Thereafter, the potential was swept from 0.4 to 0.1 V_{RHE} at 20 mV s^{-1} followed by a positive linear sweep towards 1.25 V_{RHE} at the same scan rate. The measurement was completed by cycling the potential in between 0.05 and 1.25 V_{RHE} yielding a baseline for the integration of the CO-oxidation peak. The thereby extracted charge was later used with a specific CO-stripping charge of 2·205 $\mu C \cdot cm_{Pd}^{-2}$ [58], and a minimum of 3 independent measurements were performed and their derived CO-tripping charges were averaged to calculate the electrochemical surface area (ECSA) values reported below.

Thermogravimetric analysis

The mass of Pd nanocubes dispersed on carbon was determined via thermogravimetric analysis (TGA Q500 V20.13 Build 39). Before the analysis, the sample was lyophilized. The amount of Pd and/ or Pt on carbon was measured comparing the results with the same quantity of a sample composed of only amorphous carbon. To start the measurement, a ceramic crucible was previously cleaned in aqua regia and, thereafter, thoroughly rinsed with ultrapure water and dried. Measurements were performed under air flow at a rate of 50.0 $mL \cdot min^{-1}$, starting from 30 °C and increasing the temperature with a rate of 10 °C/min up to 600 °C.

NMR analysis

NMR experiments were performed to test the catalytic properties of Pd nanocubes using as a model reaction the reduction of 4-nitrophenol to 4-aminophenol. All the NMR experiments were recorded using a Bruker FT NMR Avance III 600 MHz spectrometer equipped with a 5 mm SEF (Selective ^{19}F, ^{1}H Decoupling) probe with z-gradient coil and with an automatic sample changer (SampleJet™) with temperature control. The reduction experiments were conducted in triplicate at 25°C directly in the NMR tube in an end-point format in ultrapure water with 10% D_2O, for the lock signal. The concentrations of the different components were: 250 µM 4-nitrophenol (Alfa Aeser, code: A14376; 5 µL of 25 mM stock solution in ultrapure water), 11.2 mM sodium borohydride ($NaBH_4$, Aldrich, code 71320; 250 µL of 22.4 mM stock solution in ultrapure water 20% D_2O, vortexed 30 s before the addiction), 0.02 ppm Pd nanocubes (20 µL of 0.5 ppm stock suspension in ultrapure water) or 0.04 ppm Pd/C (10 µL of 2 ppm stock suspension in ethanol-*d6;* the concentration in ppm refers to Pd only) or 0.2 ppm Pd/C (10 µL of 10 ppm stock suspension in ethanol-*d6;* the concentration in ppm refers to Pd only). 10 µL of ethanol-*d6* were added also to the samples with 0.02 ppm Pd nanocubes in order to perform all the reactions in the identical experimental conditions. The reactions were quenched at different times by adding 40 mM HCl (Sigma Aldrich, code 258148, 20 µL of 1 M stock solution in ultrapure water) + 50 µM 3-propionic-2,2,3,3-d_4 acid (TSP, Sigma, code: 269913; 0.5 µL of 50 mM stock solution in ultrapure water) for the ^{1}H chemical shift reference; the samples where then vortexed for at least 60 s. The final volume

in the NMR tube was 500 µL. ^{1}H NMR experiments were recorded with the one-dimensional (1D) version of the NOESY (Nuclear Overhauser Effect SpectroscopY) pulse sequence and with H_2O signal presaturation. A total of 6 scans were recorded for each spectrum, with a mixing time of 10 ms and a relaxation delay of 30 s. The data were multiplied with an exponential window function with 0.3 Hz line broadening prior to Fourier transformation. The absolute concentrations of 4-nitrophenol and 4-aminophenol in solution have been obtained with high accuracy by the PULCON method[59] and using dimethyl malonic acid (Sigma, code: 89151) as external standard. The kinetics parameters (K_{app} and K_{norm}) were evaluated as reported in Ayad A.I. et al.2019[24] using the program GraphPad Prism 5.

RESULTS AND DISCUSSION

Seed-Mediated Synthesis of Pd and Pt@Pd Nanocubes

In this contribution, we report an aqueous synthesis of citrate-coated Pd nanocubes with a previously unachieved lateral size below 6 nm (Figure 1 a, b) and a narrow size polydispersity (below 15%). Moreover, the synthesis is highly versatile as it allows to finely tune the size of the nanomaterials ranging from 4 nm to 20 nm by simply changing the precursors concentration and the seeds' size (Figure 1b, c and S1-S7). The method can easily produce hundreds of milligrams in less than an hour by using a microwave reactor in a combination with multiple reaction vessels (Figure S14).

Key in the present synthesis is the use of single crystal seeds that act as templates for the subsequent growth of the cubic nanoparticles. Seed-mediated growth decouples the growth of the nanomaterial from seed formation, thereby allowing the selection of specific seed geometries. Studies of various nanocrystal syntheses indicate that specific surface atomic structures of the seeds control the final shape of the nanomaterials.[60] Pd seeds with well-defined structures such as single-crystal, multiply-twinned, stacking fault-lined, etc. can be formed by manipulating the reduction rate of Pd ions together with the other physical parameters of the synthetic protocols.[61]We tested several protocols for the synthesis of Pd seeds, but most of them provided a high polydispersity of seed morphologies (Fig. S2). This ultimately leads to high polydispersity in shape of the nanomaterial (Fig.S7). In contrast, we were able to synthesize high-quality and highly monodisperse Pt seeds. The average size of the single crystal Pt seeds used in this protocol is below 3 nm, as seen from BF-

TEM (Figure 1d and S3). The single crystal quality is further shown by HR-TEM and related FFT analysis (Figure S3d, g).

The tuning of the size of the nanocubes is achieved by changing the precursors concentration together with the seeds sizes. However, reducing agents, KBr and seed morphology in a closed vessel are crucial aspect to be controlled for allowing the formation of nanocubes as described in SI (S1-S13).

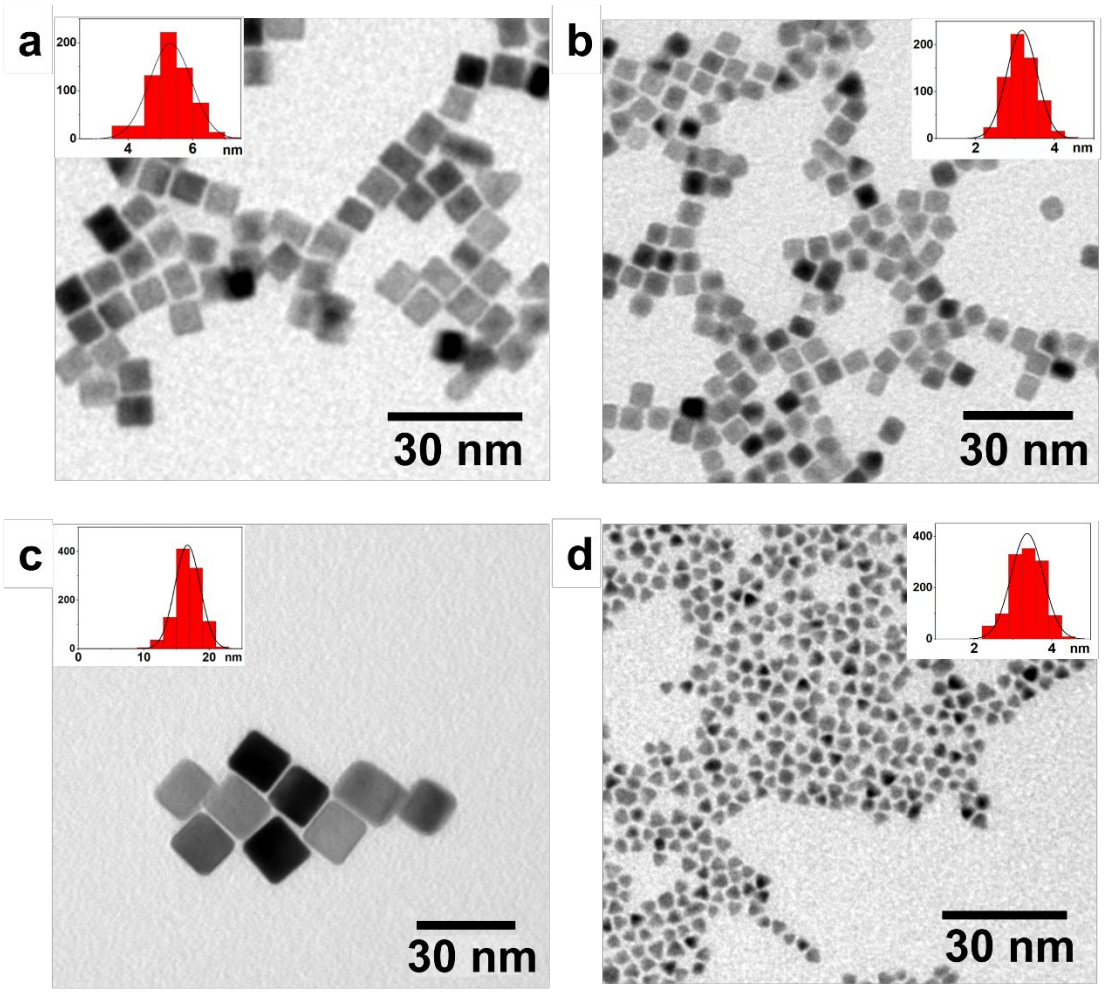

Figure 1. Morphological characterization by bright-field transmission electron microscopy (BF-TEM) of the Pt@Pd nanocubes with average lateral sizes of 5 nm (a), 3.5 nm (b) or 17 nm (c) and of the Pt seeds employed for their growth, of around 3 nm (d). The different sizes are obtained by simply changing the precursors concentration and the seeds size.

HR-TEM analysis on Pt@Pd nanocubes shows that each of them is a single-crystal, with an overall fast Fourier transform that fully matches fcc Pd (ICSD 52251), as reported in Figure S4 c-d. Given the small mismatch with the structure of fcc Pt of the cores (less than 1%) and the few percental uncertainty of this technique, it is not possible to distinguish periodic features for the Pd shells and Pt cores. HR-TEM analysis of a single Pt@Pd

nanocube in Figure 2 (a, b) shows that the nanocubes are enclosed by {100} surface facets, as expected for a cuboidal shape for an fcc structure. HAADF-STEM imaging of the Pt@Pd nanocubes demonstrate the clear presence of Pt seeds within the Pd nanocubes (as in Figure 2c), thanks to the atomic-number-contrast, and this is confirmed by compositional mapping (Figure 2 d-f). The Pt pyramidal seed is confined within the nanomaterials as depicted in Figure 2g. As the heterostructure appears monocrystalline in HRTEM, without any visible defect or strain, the Pd shell must have grown epitaxially on the pyramidal Pt seed. Thus, the Pt seeds are embedded within the Pd nanomaterials and their mono-crystallinity dictates the quality of the final shape-controlled nanocatalysts.

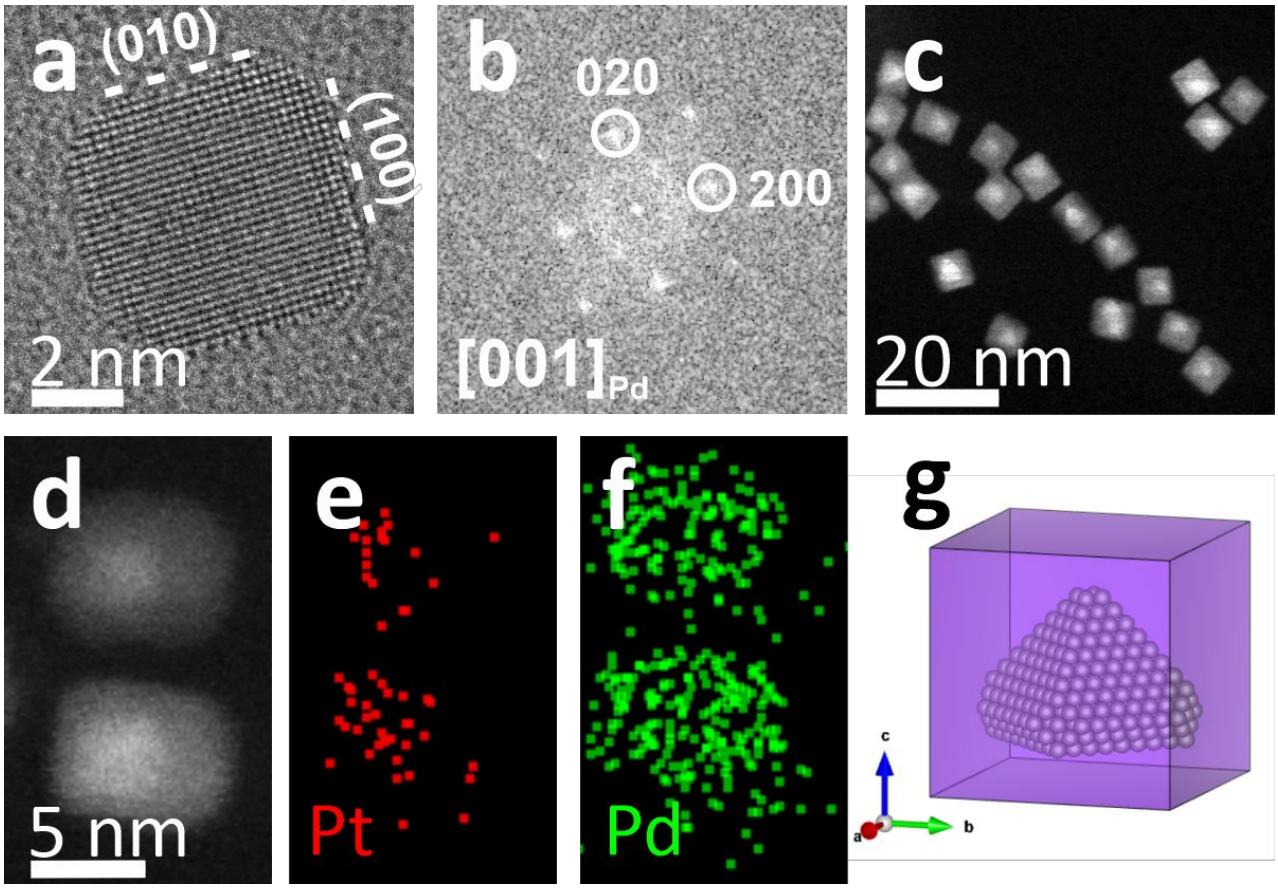

Figure 2. a) HRTEM image of one Pt@Pd nanocube in the sample, with b) FFT matching with [001]-oriented fcc Pd (ICSD 52251). c) Overview HAADF-STEM image of Pt@Pd nanocubes highlighting the presence of a high-Z pyramidal Pt core within the cubes. d) Zoom on two particles and e, f) corresponding STEM-EDS maps for Pt (red) and Pd (green). g) Schematic model of the Pt@Pd nanocubes obtained by VESTA.[62]

The presence of single-crystal seeds is necessary to obtain cubic Pd nanomaterials but it is not sufficient. The synergistic interplay of weak reducing agents, KBr and seed morphology in a closed vessel is fundamental to favour the formation of nanocubes (Figure S4-S13, Table S1). The concentration of KBr within the reaction

vessel needs to be finely tuned to achieve low polydispersity in shapes (Figure S8, Table S1). At concentrations below 10 mM of KBr, nanoparticles with higher size and shape polydispersity are obtained. (Figure S9). Likewise, if the concentration of KBr exceeds 40 mM, the synthesis becomes less controlled, with the formation of nanomaterials highly polydisperse in shape (Figures S10). Only for KBr concentrations between 10-40 mM do nanocubes form.

Oxidative etching was controlled and limited by using a closed vessel environment. High concentration of oxidants such as O_2 can reshape the seeds and favour the formation of irregular nanoparticles. In the case of an open vessel, we observed the formation of nanoparticles that are polydisperse in shape and size, likely due to the high excess of oxygen (Figure S11). Therefore, it is important to work in an environment in which the amount of oxygen is controlled and kept constant.

We also note that cube formation is sensitive to the presence of formic acid and ascorbic acid, while citric acid appears to promote colloidal stability. Ascorbic acid is present at a really low concentration (7 μM, 400 hundred times lower than formic acid), as higher concentrations lead to an excessively fast and uncontrolled reduction of Pd(II), hampering shape formation. However, ascorbic acid is necessary to promote anisotropic growth: in the absence of ascorbic acid the nanoparticles are highly polydisperse in shape (Figure S12). It seems that the concentration of formic acid is the main gauge to modulate the speed of the reduction and to achieve cubic shape. At higher concentrations of formic acid, cubes with rounded edges start to appear (Figure S13).

A final aspect of nanocube growth is that Pd(0) deposition/Pd(II) reduction appears to occur on the surface of the seeds. Nanocubes grow very rapidly since the peak at around 269 nm related to the presence of the Pd precursors (hydrated species such as $PdBr_n(H_2O)_{4-n}^{2-n}$) quickly disappears in the Uv-Vis spectrum (Figure S5). This suggests an autocatalytic reduction occurring at the surface of the seeds. This is confirmed by TEM images of nanomaterials taken before purification, that do not indicate nuclei formation during growth (Figure S9). Results of DFT calculations, which confirm these aspects, are discussed below.

Mechanism of {100}-Faceted Growth

In considering the origins of {100}-faceted nanocube formation in the presence of the various chemical species in the synthesis, we note the cube shapes are linked to three main factors: high concentrations of Br^-, presence of formic acid (HCOOH) as reducing agent, and Pd as an effective catalyst for formic acid decomposition. The contribution of ascorbic has not been taken in consideration as present in tiny concentration.[22,63–66] We also take into account the likelihood that Pd reduction (deposition) occurs on the surface of growing Pd nanocrystals. During formic acid decomposition catalyzed by bare Pd, two typical intermediates are $HCOO^-$ (formate) and $COOH^-$ (carboxyl). We studied the binding of both species to Br-covered Pd(111) and Pd(100) and found the carboxyl intermediate binds more strongly to both surfaces than the formate species (see Tables S3 and S4 in the SI). This finding is in agreement with DFT studies on bare Pd surfaces.[23,67] Thus, we hypothesize the major reactions for formic acid decomposition are:

$$HCOOH \rightarrow COOH* + H^+ + e^- \quad (2)$$

$$COOH* \rightarrow CO_2 + H^+ + e^- \quad (3)$$

where * denotes a species adsorbed on the Pd surface. These reactions provide electrons for the reduction of Pd(II) near the Pd surfaces.

To identify possible surface configurations of Pd(100) and Pd(111) with various solution-phase chemical potentials for COOH (μ_{COOH}) and Br⁻ (μ_{Br^-}), we used *ab initio* thermodynamics. This involves calculating surface energies $\gamma_{\mathrm{Pd-Br-COOH}}$ of Pd(100) and Pd(111) with various surface coverages as a function of μ_{COOH} and μ_{Br^-} using Eq. (1). We then identified the co-adsorption structures with the lowest surface energies for each pair of chemical potentials. In this way, we obtained a phase diagram of the predicted configurations of the Pd surfaces as a function of μ_{COOH} and μ_{Br^-}.

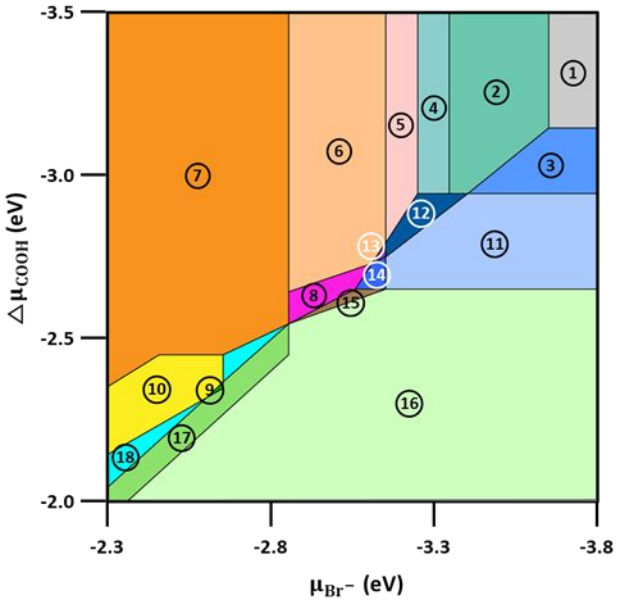

	Pd(111)		Pd(100)	
Region	θBr (ML)	θCOOH (ML)	θBr (ML)	θCOOH (ML)
1	0	0	0	0
2	0	0	1/4	0
3	0	0	0	1/3
4	1/4	0	1/4	0
5	1/3	0	1/4	0
6	1/3	0	1/3	0
7	1/3	0	1/2	0
8	1/3	0	1/4	1/8
9	1/3	1/12	1/4	1/4
10	1/3	1/12	1/2	0
11	0	1/3	0	1/3
12	0	1/3	1/4	0
13	0	1/3	1/3	0
14	0	1/3	1/4	1/8
15	0	1/2	1/4	1/8
16	0	1/2	0	1/2
17	0	1/2	1/4	1/4
18	0	1/2	1/2	0

Figure 3. Phase diagram delineating different adsorption states on Pd surfaces as a function of the Br⁻ and COOH chemical potentials. The surface coverage of Br and COOH on Pd(111) and Pd(100) for each numbered region is listed in the table. Regions for which Pd(111) contains adsorbed COOH but Pd(100) does not are highlighted.

Figure 3 shows our calculated phase diagram, which delineates the most favorable configurations for Br⁻ and COOH adsorption on the Pd surfaces as a function of $\Delta\mu_{COOH}$ and μ_{Br^-}. We use $\Delta\mu_{COOH} = \mu_{COOH} - E^{\mathrm{DFT}}_{\mathrm{COOH}}$, where $E^{\mathrm{DFT}}_{\mathrm{COOH}}$ is the energy of COOH in gas phase, for the *y*-axis of Figure 3. The corresponding surface coverage of Br⁻ and COOH in each region of Figure 3 is listed in the adjacent table. We set an upper bound

for the bromide chemical potential as $\mu_{Br^-} = -2.3$ eV because the formation of bulk $PdBr_2$ is expected above this value, according to our calculation for the experimentally observed bulk structure.[68] To understand possible thermodynamic driving forces for nanocube formation, Figure S15 shows the ratio of {111} to {100} surface energies corresponding to each region in Figure 3.

From Figure 3, we see the surfaces are devoid of COOH for sufficiently low values of $\Delta\mu_{COOH}$ (regions 2, 4 – 7). From Figure 3, we see the surfaces are devoid of COOH for sufficiently low values of $\Delta\mu_{COOH}$ (regions 2, 4 – 7) and the surfaces contain only adsorbed Br^- in regions 4 – 7. From the surface-energy ratio map in Figure S15, we see Wulff shapes ranging from truncated octahedra to cuboctahedra are predicted[69] for regions 4 – 7. It is thus evident that bromide alone does not induce nanocube formation – a finding consistent with the present experimental results. We note this result is not in agreement with that of Yoo *et al.*, who found truncated cubes could occur for sufficiently high Br^- coverage in a system with just {100} and {111} facets.[70] A major difference between their study and ours is that we probed a higher coverage of Br^- on Pd(111) (1/3 ML) than they did in their study (1/4 ML). The higher Br^- coverage (1/3 ML) stabilizes Pd(111) to a greater degree than their studied coverage of 1/4 ML, such that we do not predict cubes based on Br^- alone. From Figure S15, we see that cubes are not predicted to be thermodynamic shapes for any combination of Br^- and COOH chemical potentials, as $\gamma_{111}/\gamma_{100} \geq \sqrt{3}$ is required for perfect cubes. Thus, we sought a kinetic mechanism for nanocube formation.

Interestingly, there are five regions highlighted on Figure 3 where Pd(100) contains only adsorbed bromide and Pd(111) contains co-adsorbed bromide and carboxyl: regions 10, 12, 13 and 18. These regions are significant for nanocube or nanowire growth because adsorbed COOH can reduce Pd(II) ions. If COOH is present only on Pd(111), we expect facet-selective Pd deposition to occur on Pd(111). Facet-selective Pd deposition on Pd(111) leads to the growth of penta-twinned nanowires from decahedral seeds or nanocubes from fcc single-crystal seeds. Thus, our DFT calculations indicate the kinetic origin of cubic Pd nanoshapes is facet-selective Pd reduction/deposition on Pd(111).

Deposition on amorphous carbon

Pd -nanocubes were deposited on Vulcan at 20% *w/w* ratio and were then measured using thin-film rotating disk electrode measurements and compared to a commercial 10% Pd/C catalyst. The facile deposition of the nanocubes on amorphous carbon is enabled by the lack of of polymers and surfactant in the synthesis and performed by adding sodium hydroxide at relatively high concentration, thus favoring the detachment of citrate on the surface and, hence, the binding of the material to the carbon substrate[71]. The method provides a very well dispersed distribution of nanocrystals on the carbon substrate, which is stable for a long time without loss of shape and/ or deterioration (Figure S16). This supported Pd catalyst is henceforth denoted as cub-Pd/C. The TEM morphology of the pristine, as prepared cub-Pd/C is shown in Figure S16. After deposition on carbon (grey), the Pd NPs (dark contrast) retained their cubic shape. The Pd NPs were uniformly distributed on the carbon support and showed no apparent agglomeration. Moreover, the 20% weight fraction of these Pd NPs

on the carbon catalyst aimed in this deposition step was proven by thermogravimetric analysis (TGA) measurements in O_2 from which we derived a Pd weight percentage of 22.8% (Figure S17).

Electrochemical characterization

Pd nanocubes were deposited on amorphous carbon to increase the available surface area of the catalyst and avoid agglomeration. The choice of amorphous carbon as the supporting material is due to its electrical conductivity for electrochemical measurements together with its wide use as support material for catalytic applications in organic chemistry.

To assess the macroscopic surface properties of the Pd nanocubes, the as-prepared and carbon-supported Pd-NCs were further characterized through electrochemical measurements. Specifically, the electrochemical hydrogen underpotential deposition (Hupd) area in cyclic voltammetry (CV) measurements on palladium single crystals can indicate the presence of a dominating surface facet in the Pd-nanopartcicles' surface. To investigate these effects without the possible interference of the carbon support, CVs of the bare Pd-nanocubes in 0.1 M sulfuric acid (H_2SO_4) at a scan rate of 50 $mV \cdot s^{-1}$ were recorded (Figure 5a). Therein, the Hupd area is in good agreement with previous data in the same electrolyte for cubic Pd nanoparticles of similar size [72–76] as well as on Pd(100) single crystals.[57]

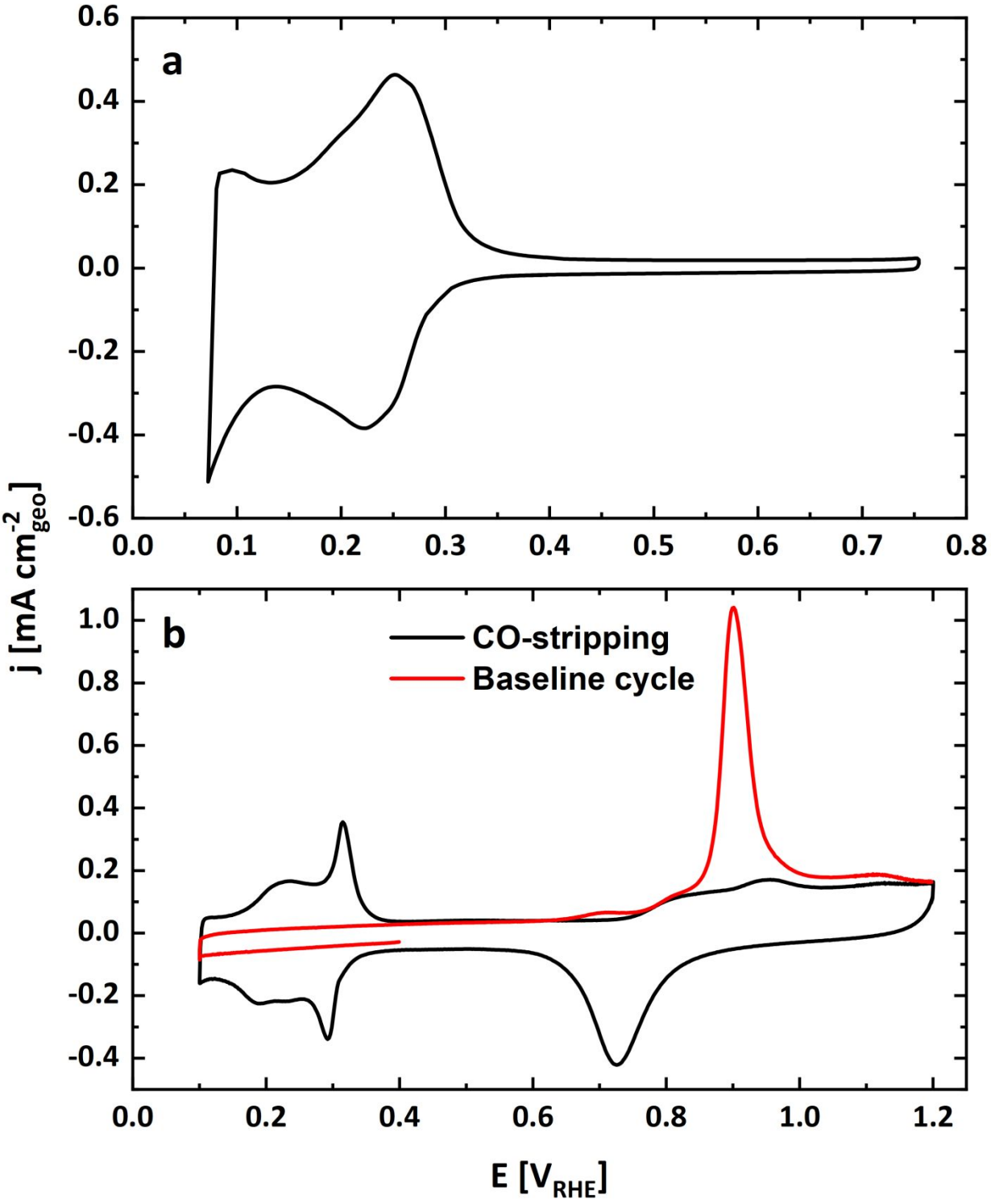

Figure 4. Cyclic voltammograms recorded on the unsupported nanocubes at 50 $mV \cdot s^{-1}$ in N_2-saturated 0.1 M H_2SO_4 at a loading of 25 $\mu g_{Pd} \cdot cm^{-2}$ (a) and CO-stripping sweeps and subsequent baseline CV at 20 mVs^{-1} in N_2-saturated, 0.5 M phosphate buffer (K_2HPO_4/KH_2PO_4) on the Pd nanocubes deposited on carbon with a loading of 10 $\mu g_{Pd} \cdot cm^{-2}$ (b).

Furthermore, Pd is well known to strongly adsorb carbon monoxide (CO) and form a monolayer that can be thereafter oxidized yielding a charge that can be used to quantify the sample's ECSA. To investigate these features on the carbon-supported Pd-nanocube catalyst, such CO-stripping experiments in an RDE configuration were performed in 0.5 M phosphate buffer (K_2HPO_4/KH_2PO_4) electrolyte, and the recorded CO-stripping and baseline CVs are displayed in Figure 5b. Here, distinct H_{upd} desorption/adsorption peaks at 0.36 and 0.34 V_{RHE} are found in the anodic and cathodic sweeps of the baseline CV, respectively, indicating that one surface facet (i.e. Pd(100)) corresponds to the majority of the available surface sites for hydrogen underpotential deposition. Moreover, the CO stripping measurements revealed a single and sharp CO-oxidation peak at ≈ 0.9 V_{RHE}, whose charge was used to calculate the ECSA value of the carbon-supported Pd nanocubes. While the CO oxidation peak position is in agreement with previous measurements on a commercial 20 % Pd/C catalyst[77] the inferred ECSA was 65 ± 3 $m^2 \cdot g_{Pd}^{-1}$, whereas the theoretical surface estimated on the basis of the Pd cubes' facet lateral length (≈ 5 nm) derived from the above TEM images (as shown in Fig. 1) is ≈ 105 $m^2 \cdot g_{Pd}^{-1}$. This disagreement between the measured ECSA and the theoretical value calculated on the basis of the nanocubes' geometry is in line with previous reports,[58] and can be explained by considering that at least one facet of the cubes (17% of the area, or 17.5 $m^2 \cdot g_{Pd}^{-1}$) is in contact with the underlaying carbon support and that some of these cubes are slightly agglomerated on the carbon surface, further preventing the contact of certain surface facets with the electrolyte. In summary, the electrochemical properties of the Pd nanocubes were found to be in agreement with previous findings in the literature, and lead us to conclude that the Pd nanocubes' shape and abundancy of Pd {100} surface facets inferred from the above TEM measurements are translated to the materials' macroscopic properties assessed by these electrochemical measurements.

Catalytic performance of Pd nanocubes

The catalytic properties of citrate-coated Pd nanocubes have been investigated to evaluate the effects in catalysis of surface structure and the absence of polymers and surfactants at the surface and have been compared to the data present in literature or with the widely used commercial Pd/C catalyst.[24,78–80] As a model reaction, the reduction of 4-nitrophenol (**S**) to 4-aminophenol (**P**) by Pd nanocubes or Pd/C in aqueous environment in the presence of an excess of sodium borohydride has been chosen. NMR has been selected as a technique as it allows the direct and absolute quantification of the compounds in solution.[81–85,86,87,24,80]
The reduction in continuous way directly into the NMR tube could not be followed because of the H_2 released by the reaction of borohydride with water and the consequent formation of bubbles (as described in SI and shown in Figure S19), which induce inhomogeneity in the NMR tube. Therefore, the experiments were performed in an end-point format, by quenching the reaction at different times with aqueous HCl in a quantity sufficient to completely quench $NaBH_4$ (Figure S20). The quenching efficiency was further confirmed by NMR (Figure S21).

As shown in Figure 5a, the amount of 4-aminophenol produced by 0.02 ppm of Pd nanocubes is largely higher than that produced by 0.2 ppm Pd/C (ppm refers to the concentration of Pd atoms) and 0.04 ppm of Pd/C (ppm refers to the concentration of Pd atoms) in the same time. The reduction efficiency **R** (Figure 5 b)**,** was calculated using the eq. 4:

$$R = \frac{C_0 - C_t}{C_o} \times 100 \qquad (4)$$

where C_0 and C_t are the initial concentration and concentration at time t of 4-nitrophenol, respectively. The plot of **R** as function of the time is shown in Figure 5b and shows that the reduction efficiency of the Pd nanocubes is much higher than that of the commercial catalyst, reaching 100% reduction after about 90 minutes. To better understand the kinetics of the different catalysts and confirm the direct dependency of the reaction from their relative amounts, we fit the data with a pseudo-first-order kinetics model using eq. 5

$$\ln \frac{C_0}{C_t} = K_{app}\, t \qquad (5)$$

where C_0 and C_t are the initial concentration and concentration at time t and *k* is the apparent rate constant. Under these conditions, the reaction proceeds with a K_{app} of 0.041 min^{-1}, 0.013 min^{-1} and 0.003 min^{-1} for the 0.02 ppm Pd nanocubes, the 0.2 ppm Pd/C and the 0.04 ppm Pd/C, respectively (Figure 5c). The correlation coefficient (R^2) value for the Pd nanocubes is 0.96 indicating that the reduction reaction of 4-nitrophenol by Pd nanocubes fits the pseudo-first-order kinetics perfectly. R^2 for the two reactions conducted with different amount of commercial Pd/C are 0.86 and 0.7, respectively, indicating a deviation from the pseudo-first-order kinetics for this commercial material.

In order to compare our results with the data present in the literature, we calculated the normalized constant, K_{norm}, using eq. 6, that take into account the concentration of sodium borohydride and the quantity of Pd used.

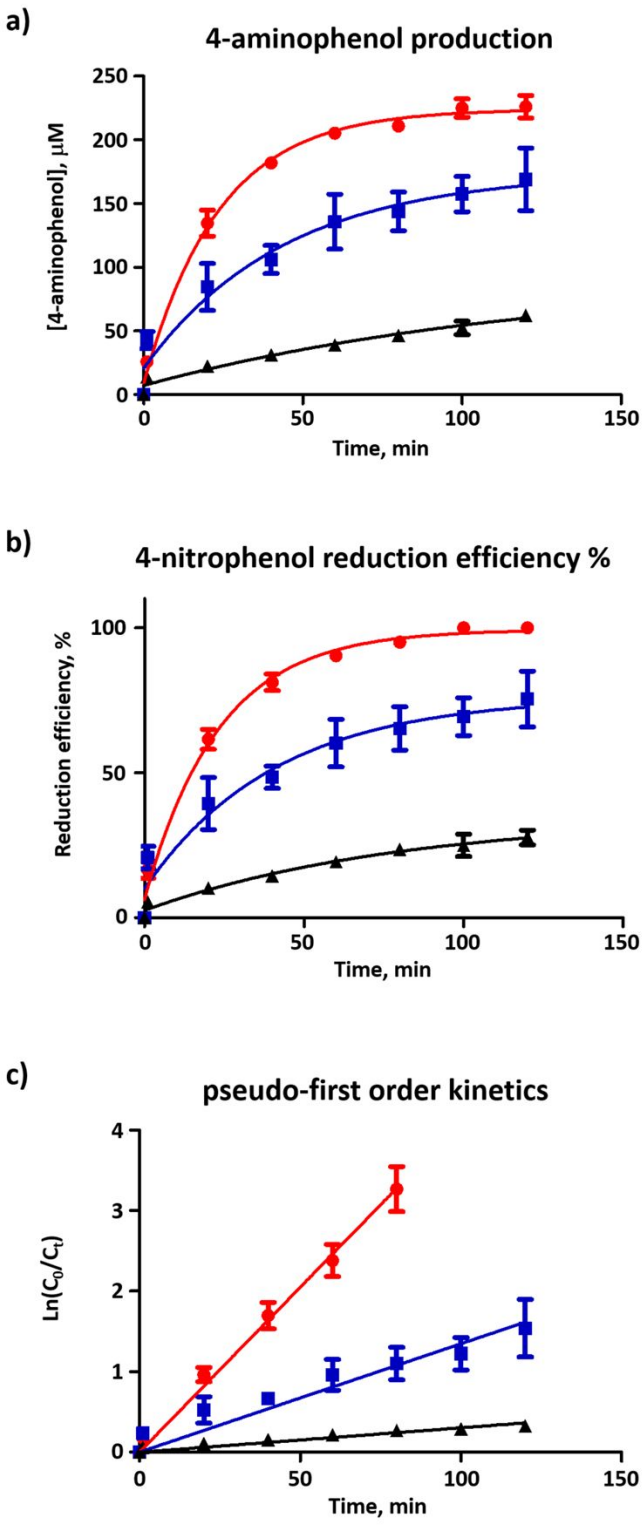

Figure 5. Catalytic performance of Pd nanocubes. 0.02 ppm Pd nanocubes, 0.2 ppm Pd/C and 0.04 ppm Pd/C are shown respectively in red, blue and black. (a) Plot of the concentration of 4-aminophenol over time of reaction. (b) Reduction efficiency in percentage of 4-nitrophenol over time. (c) Plot of the $\ln(C_0/C_t)$ over time.

$$K_{norm} = \frac{K_{app}\,(s^{-1})}{NaBH_4\,(M) \times\ Pd\,(g)} \qquad (6)$$

The values of K_{norm} for our reaction and for the reactions using different catalysts recently described in the literature are reported in Table 1. It is evident that our catalyst (Pd-nanocubes) has the highest values of K_{app} and K_{norm}. In particular, k_{norm} is 6.7 times higher than the highest value reported in the literature, proving the superior performance of Pd nanocubes thanks to the synergy between size, surface structure and the absence of unwanted chemicals at the surface.

Table 1. Comparison of rate constants of the reduction of 4-nitrophenol, catalyzed by Pd nanocubes, commercial Pd/C, and Pd NPs.

Catalyst	$NaBH_4$ eq.	K_{app} (s^{-1})	K_{norm} (s^{-1},mol^{-1},g^{-1})	Ref.
Pd-nanocubes	51	0.00068	6096726.19	this work
Pd/C	51	0.00022	200446.4	this work
Pd/C	51	0.00005	225446.4	this work
Pd-NP-B3	150	0.00060	907 020.3	**24**
AuNPs@vesicle	7	0.0026	768 745.4	**76**
Fe3O4@dextran/Pd	1000	0.000092	11 400.2	**77**
Pd nanodendrites	27.9	0.0021	681.8	**78**

In conclusion, the catalytic data prove that our Pd nanocubes prepared with a green and fast method are the most active Pd-based catalysts for 4-nitrophenol reduction described so far in the literature, with very high catalytic activity even at low loading of Pd.

CONCLUSIONS

In conclusion, we developed a fast and easy method to synthesize tuneable ultra-small Pd and Pt@Pd nanocubes with average lateral lengths below 5 nm. The synthesis requires only green, biogenic, biocompatible, and easy-to-remove compounds in aqueous solution. The role of the seed morphology is established, showing that Pt single crystal seeds are preferable to Pd seeds, as far achieving low polydispersity in shape and the absence of nanorod formation. Due to the careful design the growth process of the nanomaterial, the protocol achieves tunability, speed, and high quality of the material. The nanocubes are enclosed by {100}, as confirmed by HR-TEM and, macroscopically, by electrochemical characterization. A large production capability has also been developed using a microwave reactor that can synthesize 100 mg in less than an hour in a research laboratory setup.

The likely mechanism driving growth has been obtained by performing quantum DFT calculations that highlight the kinetic origin of cubic shape due to the facet-selectivity of the Pd reduction/deposition

preferentially on Pd(111). Moreover, we underlined both from an experimental and theoretical point of view that bromide alone does not induce nanocube formation without the synergy with formic acid.
The superior capability of these highly-controlled and high-quality nanoparticles achieved by this controlled synthesis was proved by performing the catalytic reduction of 4-nitrophenol, a reaction extensively used in organic chemistry and in industry. Compared to a commercial catalyst and data present in the literature, these Pd nanocubes exhibit superior catalytic activity that outperforms the state-of-the-art by at least a factor of 6 and a commercial Pd/C catalyst by more than one order of magnitude.

Acknowledgements

We thank Prof. Thomas J. Schmidt for fruitful discussions. We thank Mr.Alberto Pagliarini, Dr. Deborah Pedone and Dr. Doriana Debellis for providing support in performing experiments. This work is funded by the U. S. Department of Energy, Office of Basic Energy Sciences, Materials Science Division, Grant DE FG02-07ER46414 (K.F. and J.K.). J.K. acknowledges training provided by the Computational Materials Education and Training Research Traineeship, supported by the U.S. National Science Foundation (NSF) (DGE-1449785). This work used the Extreme Science and Engineering Discovery Environment (XSEDE), which is supported by NSF grant number ACI-1548562 (K.F. and J.K.).

Competing financial interests

The authors declare no competing financial interests.

Author Contributions

VM, PPP and MM conceived the synthetic procedure for Pd NPs syntheses. VM, TP, GU performed the syntheses and the characterization of Pd NPs. MM and MV conceived the application of Pd NPs

in catalysis. MV, TB, FB designed and performed the catalysis experiments. VM and RB performed TEM experiments and analysis. RB performed HR-TEM experiments and analysis. JD and JS conceived and performed the electrochemistry experiments. KF and JK conceived the DFT calculations. JK performed the DFT calculations. MM and KF conceived the project and analysed data. All the authors contributed to the preparation of the manuscript.

REFERENCES

1. De Luca, E. *et al.* Multifunctional Platinum@BSA-Rapamycin Nanocarriers for the Combinatorial Therapy of Cerebral Cavernous Malformation. *ACS Omega* **3**, 15389–15398 (2018).
2. Xia, Y. & Yang, X. Toward Cost-Effective and Sustainable Use of Precious Metals in Heterogeneous Catalysts. *Acc. Chem. Res.* **50**, 450–454 (2017).
3. Guarnieri, D. *et al.* Particle size affects the cytosolic delivery of membranotropic peptide-functionalized platinum nanozymes. *Nanoscale* **9**, 11288–11296 (2017).
4. Leso, V. & Iavicoli, I. Palladium Nanoparticles: Toxicological Effects and Potential Implications for Occupational Risk Assessment. *Int. J. Mol. Sci.* **19**, 503 (2018).
5. Huang, H. *et al.* One-Pot Synthesis of Penta-twinned Palladium Nanowires and Their Enhanced Electrocatalytic Properties. *ACS Appl. Mater. Interfaces* **9**, 31203–31212 (2017).
6. Xie, X., Liao, J., Shao, X., Li, Q. & Lin, Y. The Effect of shape on Cellular Uptake of Gold Nanoparticles in the forms of Stars, Rods, and Triangles. *Sci. Rep.* **7**, 1–9 (2017).
7. Koo, W. T. *et al.* Accelerating Palladium Nanowire H2 Sensors Using Engineered Nanofiltration. *ACS Nano* **11**, 9276–9285 (2017).
8. Moglianetti, M. *et al.* Intracellular Antioxidant Activity of Biocompatible Citrate-Capped Palladium Nanozymes. *Nanomaterials* **10**, 99 (2020).
9. Liz-Marzán, L. M. & Grzelczak, M. Growing anisotropic crystals at the nanoscale. *Science (80-.).* **356**, 1120–1121 (2017).
10. Gatto, F. *et al.* PMA-Induced THP-1 Macrophage Differentiation is Not Impaired by Citrate-Coated Platinum Nanoparticles. *Nanomaterials* **7**, 332 (2017).
11. Zhang, H., Jin, M., Xiong, Y., Lim, B. & Xia, Y. Shape-controlled synthesis of Pd nanocrystals and their catalytic applications. *Acc. Chem. Res.* **46**, 1783–1794 (2013).
12. Figueroa-Cosme, L. *et al.* Synthesis of Palladium Nanoscale Octahedra through a One-Pot, Dual-Reductant Route and Kinetic Analysis. *Chem. - A Eur. J.* **24**, 6133–6139 (2018).
13. Long, N. V., Thi, C. M., Yong, Y., Nogami, M. & Ohtaki, M. Platinum and Palladium Nano-Structured Catalysts for Polymer Electrolyte Fuel Cells and Direct Methanol Fuel Cells. *J. Nanosci. Nanotechnol.* **13**, 4799–4824 (2013).

14. Chen, A. & Ostrom, C. Palladium-Based Nanomaterials: Synthesis and Electrochemical Applications. *Chem. Rev.* **115**, 11999–12044 (2015).

15. Xiong, Y. *et al.* Size-dependence of surface plasmon resonance and oxidation for Pd nanocubes synthesized via a seed etching process. *Nano Lett.* **5**, 1237–1242 (2005).

16. Liu, X. *et al.* The oxidation of carbon monoxide over the palladium nanocube catalysts: Effect of the basic-property of the support. *Catal. Commun.* **46**, 213–218 (2014).

17. Martins, J. *et al.* CO2 hydrogenation with shape-controlled Pd nanoparticles embedded in mesoporous silica: Elucidating stability and selectivity issues. *Catal. Commun.* **58**, 11–15 (2015).

18. Gustafson, J. *et al.* The Role of Oxides in Catalytic CO Oxidation over Rhodium and Palladium. *ACS Catal.* **8**, 4438–4445 (2018).

19. Guo, S. & Wang, E. Noble metal nanomaterials: Controllable synthesis and application in fuel cells and analytical sensors. *Nano Today* vol. 6 240–264 (2011).

20. Swain, S. *et al.* Controlled Synthesis of Palladium Nanocubes as an Efficient Nanocatalyst for Suzuki-Miyaura Cross-Coupling and Reduction of p-Nitrophenol. *Langmuir* **36**, 5208–5218 (2020).

21. Cui, Z. & Bai, X. Structure-controlled synthesis of palladium concave nanocubes via CTAB-assisted reduction for methanol electro-oxidation. *J. Mater. Sci.* **55**, 4808–4819 (2020).

22. Shao, M., Odell, J., Humbert, M., Yu, T. & Xia, Y. Electrocatalysis on shape-controlled palladium nanocrystals: Oxygen reduction reaction and formic acid oxidation. *J. Phys. Chem. C* **117**, 4172–4180 (2013).

23. Choi, S. Il *et al.* A Comprehensive Study of Formic Acid Oxidation on Palladium Nanocrystals with Different Types of Facets and Twin Defects. *ChemCatChem* **7**, 2077–2084 (2015).

24. Iben Ayad, A. *et al.* 'Water soluble' palladium nanoparticle engineering for C-C coupling, reduction and cyclization catalysis. *Green Chem.* **21**, 6646–6657 (2019).

25. Teng, X., Han, W.-Q., Ku, W. & Hücker, M. Synthesis of Ultrathin Palladium and Platinum Nanowires and a Study of Their Magnetic Properties. *Angew. Chemie* **120**, 2085–2088 (2008).

26. Hai-Wei, L. *et al.* Ultrathin Te nanowires: An excellent platform for controlled synthesis of ultrathin platinum and palladium nanowires/nanotubes with very high aspect ratio. *Adv. Mater.* **21**, 1850–1854 (2009).

27. Siril, P. F., Lehoux, A., Ramos, L., Beaunier, P. & Remita, H. Facile synthesis of palladium nanowires by a soft templating method. *New J. Chem.* **36**, 2135–2139 (2012).

28. Xu, D., Liu, X., Han, M. & Bao, J. Facile synthesis of ultrathin single-crystalline palladium nanowires with enhanced electrocatalytic activities. *Chem. Commun.* **52**, 12996–12999 (2016).

29. Cui, Z., Bai, X. & Liu, T. Effect of Hexadecylpyridinium Bromide (HDPB) on Morphology and Electrocatalytic Performance of Porous Palladium Nanoparticles. *ChemistrySelect* **5**, 1109–1114 (2020).

30. Wang, X. *et al.* Palladium-platinum core-shell icosahedra with substantially enhanced activity and durability towards oxygen reduction. *Nat. Commun.* **6**, 1–8 (2015).

31. Kettemann, F. *et al.* Reliable palladium nanoparticle syntheses in aqueous solution: The importance of understanding precursor chemistry and growth mechanism. *CrystEngComm* **17**, 1865–1870 (2015).

32. Montiel, M. A., Vidal-Iglesias, F. J., Montiel, V. & Solla-Gullón, J. Electrocatalysis on shape-controlled metal nanoparticles: Progress in surface cleaning methodologies. *Curr. Opin. Electrochem.* **1**, 34–39 (2017).

33. Yang, T.-H., Shi, Y., Janssen, A. & Xia, Y. Surface Capping Agents and Their Roles in Shape-Controlled Synthesis of Colloidal Metal Nanocrystals. *Angew. Chemie Int. Ed.* **59**, 15378–15401

(2020).

34. Navas, M. P. & Soni, R. K. Bromide (Br −) ion-mediated synthesis of anisotropic palladium nanocrystals by laser ablation. *Appl. Surf. Sci.* **390**, 718–727 (2016).

35. Castelli, A. *et al.* Anisotropic nanoparticles: general discussion Faraday Discussions. **5**, 229–254 (2016).

36. Lim, B. *et al.* Shape-Controlled Synthesis of Pd Nanocrystals in Aqueous Solutions. *Adv. Funct. Mater.* **19**, 189–200 (2009).

37. Liu, X. *et al.* Facile Synthesis of Pd Nanocubes with Assistant of Iodide and Investigation of Their Electrocatalytic Performances Towards Formic Acid Oxidation. *Nanomaterials* **9**, 375 (2019).

38. Jang, K. *et al.* Three-dimensional atomic mapping of ligands on palladium nanoparticles by atom probe tomography. *Nat. Commun.* **12**, 1–10 (2021).

39. Kinoshita, K. Particle Size Effects for Oxygen Reduction on Highly Dispersed Platinum in Acid Electrolytes. *J. Electrochem. Soc.* **137**, 845–848 (2019).

40. Kim, M. J., Alvarez, S., Chen, Z., Fichthorn, K. A. & Wiley, B. J. Single-Crystal Electrochemistry Reveals Why Metal Nanowires Grow. *J. Am. Chem. Soc.* **140**, 14740–14746 (2018).

41. Yang, T. H., Zhou, S., Zhao, M. & Xia, Y. Quantitative Analysis of the Multiple Roles Played by Halide Ions in Controlling the Growth Patterns of Palladium Nanocrystals. *ChemNanoMat* **6**, 576–588 (2020).

42. Yang, T. H. *et al.* Toward a quantitative understanding of the reduction pathways of a salt precursor in the synthesis of metal nanocrystals. *Nano Lett.* **17**, 334–340 (2017).

43. Kresse, G. & Hafner, J. Ab Initio molecular dynamics for liquid metals. *Phys. Rev. B* **47**, 558–561 (1993).

44. Kresse, G. & Hafner, J. Ab Initio molecular-dynamics simulation of the liquid-metal–amorphous-semiconductor transition in germanium. *Phys. Rev. B* **49**, 14251–14269 (1994).

45. Kresse, G. & Furthmüller, J. Efficient iterative schemes for ab Initio total-energy calculations using a plane-wave basis set. *Phys. Rev. B* **54**, 11169–11186 (1996).

46. Blöchl, P. E. Projector augmented-wave method. *Phys. Rev. B* **50**, 17953 (1994).

47. Kresse, G. & Joubert, D. From ultrasoft pseudopotentials to the projector augmented-wave method. *Phys. Rev. B* **59**, 1758–1775 (1999).

48. Perdew, J. P., Burke, K. & Ernzerhof, M. Generalized gradient approximation made simple. *Phys. Rev. Lett.* **77**, 3865–3868 (1996).

49. Monkhorst, H. J. & Pack, J. D. Special points for Brillouin-zone integrations. *Phys. Rev. B* **13**, 5188 (1976).

50. Grimme, S. Semiempirical GGA-type density functional constructed with a long-range dispersion correction. *J. Comput. Chem.* **27**, 1787–1799 (2006).

51. Ruiz, V. G., Liu, W., Zojer, E., Scheffler, M. & Tkatchenko, A. Density-functional theory with screened van der Waals interactions for the modeling of hybrid inorganic-organic systems. *Phys. Rev. Lett.* **108**, 146103 (2012).

52. Pašti, I. A. & Mentus, S. V. Halogen adsorption on crystallographic (1 1 1) planes of Pt, Pd, Cu and Au, and on Pd-monolayer catalyst surfaces: First-principles study. *Electrochim. Acta* **55**, 1995–2003 (2010).

53. Vorotnikov, V., Mpourmpakis, G. & Vlachos, D. G. DFT study of furfural conversion to furan, furfuryl alcohol, and 2-methylfuran on Pd(111). *ACS Catal.* **2**, 2496–2504 (2012).

54. Quon, S. *et al.* Role of Pt atoms on Pd(1 1 1) surface in the direct synthesis of hydrogen peroxide: Nano-catalytic experiments and DFT calculations. *J. Catal.* **368**, 237–247 (2018).

55. Xu, L., Bhandari, S., Chen, J., Glasgow, J. & Mavrikakis, M. Chloroform Hydrodechlorination on Palladium Surfaces: A Comparative DFT Study on Pd(111), Pd(100), and Pd(211). *Top. Catal.* **63**, 762–776 (2020).

56. Schmidt, T. J. *et al.* Characterization of High-Surface-Area Electrocatalysts Using a Rotating Disk Electrode Configuration. *J. Electrochem. Soc.* **145**, 2354–2358 (1998).

57. Hara, M., Linke, U. & Wandlowski, T. Preparation and electrochemical characterization of palladium single crystal electrodes in 0.1 M H2SO4 and HClO4: Part I. Low-index phases. *Electrochim. Acta* **52**, 5733–5748 (2007).

58. Mittermeier, T., Weiß, A., Gasteiger, H. A. & Hasché, F. Monometallic Palladium for Oxygen Reduction in PEM Fuel Cells: Particle-Size Effect, Reaction Mechanism, and Voltage Cycling Stability. *J. Electrochem. Soc.* **164**, F1081–F1089 (2017).

59. Wider, G. & Dreier, L. Measuring Protein Concentrations by NMR Spectroscopy. *J. Am. Chem. Soc.* **128**, 2571–2576 (2006).

60. Yang, T., Zhou, S., Zhao, M. & Xia, Y. Quantitative Analysis of the Multiple Roles Played by Halide Ions in Controlling the Growth Patterns of Palladium Nanocrystals. *ChemNanoMat* **6**, 576–588 (2020).

61. Xiong, Y. & Xia, Y. Shape-controlled synthesis of metal nanostructures: The case of palladium. *Adv. Mater.* **19**, 3385–3391 (2007).

62. Momma, K. & Izumi, F. VESTA 3 for three-dimensional visualization of crystal, volumetric and morphology data. *J. Appl. Crystallogr.* **44**, 1272–1276 (2011).

63. Zhu, Y., Khan, Z. & Masel, R. I. The behavior of palladium catalysts in direct formic acid fuel cells. *J. Power Sources* **139**, 15–20 (2005).

64. Nishimura, K., Kunimatsu, K., Machida, K. ichi & Enyo, M. Electrocatalysis of Pd + Au alloy electrodes. Part IV. IR spectroscopic studies on the surface species derived from formaldehyde and formate in alkaline solutions. *J. Electroanal. Chem.* **260**, 181–192 (1989).

65. Zheng, T. *et al.* The structure of formate species on Pd(111) calculated by density functional theory and determined using low energy electron diffraction. *Surf. Sci.* **574**, 166–174 (2005).

66. Pronkin, S., Hara, M. & Wandlowski, T. Electrocatalytic properties of Au(111)-Pd quasi-single-crystal film electrodes as probed by ATR-SEIRAS. *Russ. J. Electrochem.* **42**, 1177–1192 (2006).

67. Herron, J. A., Scaranto, J., Ferrin, P., Li, S. & Mavrikakis, M. Trends in formic acid decomposition on model transition metal surfaces: A density functional theory study. *ACS Catal.* **4**, 4434–4445 (2014).

68. Brodersen, K., Thiele, G. & Gaedcke, H. Die Konstitution des Palladium(II)-bromids. *Zeitschrift fuer Anorg. und Allg. Chemie* **348**, 162–167 (1966).

69. Fichthorn, K. A. *et al.* Understanding the Solution-Phase Growth of Cu and Ag Nanowires and Nanocubes from First Principles. *Langmuir* **37**, 4419–4431 (2021).

70. Yoo, S. H., Lee, J. H., Delley, B. & Soon, A. Why does bromine square palladium off? An ab initio study of brominated palladium and its nanomorphology. *Phys. Chem. Chem. Phys.* **16**, 18570–18577 (2014).

71. Hornberger, E. *et al.* Seed-Mediated Synthesis and Catalytic ORR Reactivity of Facet-Stable, Monodisperse Platinum Nano-Octahedra. *ACS Appl. Energy Mater.* **4**, 9542–9552 (2021).

72. Erikson, H. *et al.* Oxygen electroreduction on carbon-supported Pd nanocubes in acid solutions. *Electrochim. Acta* **188**, 301–308 (2016).

73. Erikson, H. *et al.* Electrochemical reduction of oxygen on palladium nanocubes in acid and alkaline

solutions. *Electrochim. Acta* **59**, 329–335 (2012).

74. Garnier, E., Vidal-Iglesias, F. J., Feliu, J. M. & Solla-Gullón, J. Surface Structure Characterization of Shape and Size Controlled Pd Nanoparticles by Cu UPD: A Quantitative Approach. *Front. Chem.* **7**, 527 (2019).

75. Hoshi, N., Kagaya, K. & Hori, Y. Voltammograms of the single-crystal electrodes of palladium in aqueous sulfuric acid electrolyte: Pd(S)-[n(111)×(111)] and Pd(S)-[n(100)×(111)]. *J. Electroanal. Chem.* **485**, 55–60 (2000).

76. Hoshi, N., Kuroda, M. & Hori, Y. Voltammograms of stepped and kinked stepped surfaces of palladium: Pd(S)-[n(111)×(100)] and Pd(S)-[n(100)×(110)]. *J. Electroanal. Chem.* **521**, 155–160 (2002).

77. Diercks, J. S. *et al.* An Online Gas Chromatography Cell Setup for Accurate CO 2 -Electroreduction Product Quantification . *J. Electrochem. Soc.* **168**, 064504 (2021).

78. Lara, L. R. S. *et al.* The catalytic evaluation of in situ grown Pd nanoparticles on the surface of Fe3O4@dextran particles in the p-nitrophenol reduction reaction. *RSC Adv.* **5**, 8289–8296 (2015).

79. Mourdikoudis, S. *et al.* Highly porous palladium nanodendrites: Wet-chemical synthesis, electron tomography and catalytic activity. *Dalt. Trans.* **48**, 3758–3767 (2019).

80. Wu, G. *et al.* A facile approach for the reduction of 4-nitrophenol and degradation of congo red using gold nanoparticles or laccase decorated hybrid inorganic nanoparticles/polymer-biomacromolecules vesicles. *Mater. Sci. Eng. C* **94**, 524–533 (2019).

81. Podgorskii, V. V., Mikhalev, A. S. & Kalabin, G. A. Quantitative nmr spectroscopy for quality control of drugs and pharmaceuticals. *Pharm. Chem. J.* **3**, 194–197 (2011).

82. Rundlöf, T., McEwen, I., Johansson, M. & Arvidsson, T. Use and qualification of primary and secondary standards employed in quantitative 1H NMR spectroscopy of pharmaceuticals. *J. Pharm. Biomed. Anal.* **93**, 111–117 (2014).

83. Dalvit, C., Caronni, D., Mongelli, N., Veronesi, M. & Vulpetti, A. NMR-based quality control approach for the identification of false positives and false negatives in high throughput screening. *Curr. Drug Discov. Technol.* **3**, 115–124 (2006).

84. Sreeramulu, S. *et al.* NMR quality control of fragment libraries for screening. *J. Biomol. NMR* **74**, 555–563 (2020).

85. Popov, A. I. & Hallenga, K. *Modern NMR techniques and their application in chemistry*. (M. Dekker, 1991).

86. Butler, B. J., Thomas, D. S., Hook, J. M. & Harper, J. B. NMR spectroscopy to follow reaction progress in ionic liquids. *Magn. Reson. Chem.* **54**, 423–428 (2016).

87. Bernstein, M. A., Štefinović, M. & Sleigh, C. J. Optimising reaction performance in the pharmaceutical industry by monitoring with NMR. *Magn. Reson. Chem.* **45**, 564–571 (2007).